The effects of crossing trajectories on the dispersion of particles in a turbulent flow

By M. R. WELLS† AND D. E. STOCK

Department of Mechanical Engineering, Washington State University,
Pullman, Washington 99164

The effects of 'crossing trajectories' and inertia on the dispersion of particles suspended in a field of grid-generated turbulence were investigated experimentally. The effect of particle trajectories crossing the trajectories of fluid elements, under the influence of a potential field (usually gravity), is to force the particles from one region of highly correlated flow to another. In this manner, particles lose velocity correlation more rapidly than the corresponding fluid points and as a result disperse less.

A homogeneous decaying turbulent field was created behind a square biplanar grid in a wind tunnel. Particles were charged by a corona discharge then passed into the test section through a small plastic tube. A uniform electric field within the test section was used to simulate the effect of gravity, forcing the charged particles out of regions of correlated fluid at a higher than normal rate, therefore inducing the effects of crossing trajectories. Two sizes of glass beads (5 μm and 57 μm diameter) were employed in order to observe inertial effects. Laser-Doppler anemometry was used to measure particle mean-square displacement, autocorrelation coefficient, and mean-square velocity, from which dispersion coefficients were calculated.

For the two particle sizes used in the tests, it was found that the particle diffusion coefficient, after a suitably long time from their release, was influenced primarily by the effect of crossing trajectories. Only in the particle mean-square velocity was the particle inertia seen to have any effect. The ratio of the particle relaxation time to the Kolmogoroff timescale was found to be a good indicator for the effects of particle inertia.

1. Introduction

Paralleling development of numerical schemes to predict turbulent flow fields have been attempts to predict the dispersion of particles (solid, liquid, or bubbles) in such fields (Reeks 1977; Riley & Patterson 1974; Meek & Jones 1973; Berlemont & Gouesbet 1981). Unfortunately, numerical predictions have been plagued by a lack of experimental data to validate the schemes.

Motion of particles in turbulent flow is governed by the coupled effects of the turbulent flow field, particle inertia and the particle's free-fall velocity (crossing-trajectory effects). All three of these effects could influence the dispersion of heavy particles, while the dispersion of light particles is controlled predominantly by the effects of the turbulent flow field. In the study of particle dispersion it has been difficult to separate experimentally the effects of inertia from that of crossing trajectories, since, under the influence of the Earth's gravitational field, a particle's free fall velocity increases as its inertia increases. It is necessary to isolate the

† Present address: Amoco Production Research, Tulsa, OK.

individual consequences of particle inertia and the particle's free-fall velocity on the dispersion process to fully understand the mechanism of heavy particle dispersion.

Yudine (1959) hypothesized the several effects of a particle's free-fall velocity on its dispersion rate. The most significant of these, as borne out by subsequent investigations, is that termed by Yudine the 'effect of crossing trajectories'. This effect results from a heavy particle's tendency to change its fluid neighbourhood continually owing to its finite free-fall velocity. A heavy particle, influenced by an external potential force field such as gravity, falls from one eddy to another at a rate faster than the average eddy-decay rate. In contrast, a light particle (or a fluid point) will generally remain within an eddy until the eddy decays. As a result, the heavy particle tends to lose velocity correlation more rapidly than a light particle. Since the particle correlation time is directly related to its dispersion coefficient, heavy particles disperse less.

The effect of a constant free-fall velocity on the dispersion of particles in a turbulent flow is then to decrease the particle dispersion coefficient by approximately the inverse of the free-fall velocity (Csanady 1963). This decrease is evidently due to the effects of crossing trajectories, and dominates the dispersion process when the free-fall velocity is of the order of magnitude of the turbulent fluctuating velocity or larger. The significance of the crossing-trajectories effect is not clear, however, when the free-fall velocity is less than the turbulent velocity. This is borne out in the apparent lack of coincidence between the theoretical models (Meek & Jones 1973; Nir & Pismen 1979) and the existing light-particle experimental data (Snyder & Lumley 1971).

The effect of particle inertia, characterized by the particle relaxation time, is to cause the particle r.m.s. velocity to be less than that of the fluid (Snyder & Lumley 1971). Since an increase in inertia causes the particle to lag behind the fluctuating fluid velocity, a second effect of inertia is to increase the particle velocity correlation time (integral timescale) (Chao 1965). The effect of inertia on particle dispersion is therefore obscured by the fact that the dispersion coefficient is the product of the particle mean-square fluctuating velocity and its integral timescale. The results of the studies of Reeks (1977) and Pismen & Nir (1978), however, indicate that the dispersion of small particles ($\tau_p < 0.1$ s), in the absence of a free-fall velocity, is only weakly influenced by particle inertia. The proper scaling factor to determine the significance of the inertia effect is also unclear. Snyder & Lumley (1971) and Calabrese & Middleman (1979) imply the ratio of the particle relaxation time τ_p, to the fluid Kolmogoroff timescale τ_k be used, while Csanady (1963) and Meek & Jones (1973) suggest use of the ratio of τ_p to the Eulerian fluid integral timescale T_E. In the present study, the ratio of τ_p/τ_k, which correlates with how closely the particle will follow the fluctuating fluid velocity, was used as a guide in selecting particles.

2. Background

Taylor (1921) postulated a fundamentally correct theory describing the statistical dispersion of fluid points in a stationary homogeneous turbulent flow. He derived the following well-known equation for the fluid dispersion coefficient $D_{fij}(\tau)$ in terms of Lagrangian velocities $v_i(t)$:

$$D_{fij}(\tau) = \frac{1}{2}\frac{\mathrm{d}}{\mathrm{d}\tau}\overline{Y_i(\tau)\,Y_j(\tau)} \quad (i,j = 1,2,3) \tag{1}$$

$$= v'^2 \int_0^\tau R_{Lij}(s)\,\mathrm{d}s,$$

where $\overline{Y^2(\tau)}$ is the variance of the dispersion as a function of time and $R_{Lij}(s)$, the Lagrangian fluid-velocity correlation function, is given by

$$R_{Lij}(s) = \frac{\overline{v_i(t)\, v_j(t+s)}}{v'^2}.\tag{2}$$

Thus

$$\overline{Y^2(T)} = 2v'^2 \int_0^T \int_0^{t'} R_{Lii}(\tau)\, \mathrm{d}\tau\, \mathrm{d}t',\tag{3}$$

where v' is the r.m.s turbulent velocity. In the present study, the indices $i = 1, 2, 3$ represent streamwise, vertical and horizontal cross-stream directions respectively. These equations are equally applicable to the dispersion of particles, provided that the Lagrangian velocities and integral scales are interpreted to be those of the particle. The fact that Taylor's formulation uses Lagrangian statistical correlations severely restricts its practical use, because the relationship between Lagrangian variables and the more easily obtained Eulerian variables is not known *a priori*.

Yudine (1959) considered the physical consequences for finite free-fall velocities on the dispersion of heavy particles. Using the theories of Kolmogoroff (1941), he formulated upper and lower limits for the changes in the dispersion coefficient due to a heavy particle's free-fall velocity v_d. He then concluded that, for large v_d, dispersion coefficients take on an asymptotic form inversely proportional to the terminal velocity.

Csanady (1963) examined the differences between dispersion of heavy particles and fluid points. He considered the particle inertia to be sufficiently small for the particle to follow the fluid-velocity fluctuations while the particle's weight was considered heavy enough so that it would experience a free-fall velocity due to gravity. Csanady reasoned that the effect of a large constant free-fall velocity on particle diffusion is seen by substituting the Eulerian correlation function for the Lagrangian function into Taylor's relation (1). By considering the probable shape of the correlation isoclines for the Lagrangian and Eulerian correlation coefficients (for large v_d), he was able to construct two relations for the particle dispersion coefficients parallel to (longitudinal) and normal to (lateral) the direction of the drift velocity. Comparing these results with those for fluid point dispersion, he arrived at the following equations involving ratios of the longitudinal (11) and lateral (22) coefficients respectively

$$\frac{D_{p11}(\tau)}{D_{f11}(\tau)} = \left[1 + \frac{\beta^2 v_d^2}{v'^2}\right]^{-\frac{1}{2}},\tag{4}$$

$$\frac{D_{p22}(\tau)}{D_{f22}(\tau)} = \left[1 + \frac{4\beta^2 v_d^2}{v'^2}\right]^{-\frac{1}{2}},\tag{5}$$

where $D_p(\tau)$ is the particle dispersion coefficient, v'^2 is the mean-square velocity in the direction of v_d, and $\beta = v' T_L / L_E$ relates the Lagrangian integral timescale T_L, and the Eulerian integral lengthscale L_E. In this case, gravitational acceleration is assumed to be in the positive 11-direction. Here it can be seen that the effect of v_d is to decrease the dispersion coefficient proportionately to its inverse. Csanady (1964) also attempted to demonstrate experimentally the effect of crossing trajectories by dropping clusters of heavy particles from a high tower into a turbulent atmosphere. Although little data were accumulated and large uncertainties were present, the results were quantitatively consistent with his predictions.

Snyder & Lumley (1971) measured the Lagrangian autocorrelation experimentally using particles of various sizes and densities ranging from light particles that would

closely follow the fluid fluctuations to heavy particles that would experience both inertia and crossing-trajectory effects. Their data clearly showed a decrease in mean-square displacement, hence in particle dispersion, with an increase in gravitational free-fall velocity. The difference in particle autocorrelations and mean-square displacements they attributed mainly to the crossing-trajectory effects. Snyder & Lumley also compared the particle turbulence decay to the fluid turbulence decay, and found that the particle turbulence decayed more rapidly, most likely due to inertia effects.

Calabrese & Middleman (1979) photographically measured the degree of radial dispersion of medium-sized particles from a point source in the core region of a fully developed turbulent pipe flow of water. Medium-sized particles they defined by $\eta_k < d_p < L_L$, where η_k, d_p and L_L are the Kolmogoroff lengthscale, particle diameter and Lagrangian lengthscale respectively. They were able to calculate the radial mean-square particle displacement directly to find that both heavy and buoyant particles experienced a decrease in mean-square displacement due to the crossing-trajectory effects. Comparing their data with that of Snyder & Lumley, they found good agreement between both the Lagrangian integral scales and the eddy diffusivities of the two studies.

No attempt has been made to isolate experimentally the effects of inertia and crossing trajectories on the dispersion process. The aim of this study was to examine experimentally the effects of crossing trajectories and inertia on particle dispersion independently, particularly when the particle gravitational free-fall velocity was less than the fluid r.m.s. velocity.

3. Experimental design and apparatus

The present study examines the effect of crossing trajectories over a variety of drift velocities, from $v_d = 0$, no effect, to a point where the crossing-trajectory effects dominate the dispersion process. Since the particle drift velocity v_d is a function of particle relaxation time τ_p and acceleration due to the potential field, usually gravity, the magnitude of either of these two parameters dictates the extent of the effect of crossing trajectories. To vary τ_p over a wide range with sufficient resolution would require a large number of particles grouped according to various diameter and density combinations. Such an approach would be extremely costly and time-consuming. In addition, since the inertia effect is also a function of τ_p, it would be impossible to examine the effects of crossing trajectories without the influence of particle inertia. However, by varying the strength of the potential field, a very fine resolution in the drift velocity may be obtained, isolating the effects of crossing trajectories and inertia. For these reasons the second method was selected for this study.

The potential field used was a uniform electric field set up between two parallel plates in a wind tunnel. The electric field strength was sufficient to achieve free-fall velocities as high as four times that due to gravity, and by reversing the polarity of the electric field the gravitational effects could be nullified. Also, by selecting two types of particles, high τ_p and low τ_p, inertia effects were examined independently of crossing-trajectories effects.

3.1. *Flow field*

Theoretically, this study required that the flow field used be isotropic and stationary. Unfortunately, such a flow does not exist in nature; however, experimental evidence suggests that grid-generated turbulent flows approximate these requirements. This

approximately isotropic field decreases in intensity in the direction of the mean flow; that is, the mean-square turbulent velocity decays with time. For this reason grid-generated turbulent fields are frequently termed homogeneous decaying turbulence. Grid flows are relatively simple to construct and have been used extensively in laboratory studies; consequently, grid flows have been very well documented. Because of the simplicity of construction and the close approximation to isotropic flow, grid-generated turbulence was selected for this study. In addition, it was useful to compare the results of this experiment with those of Snyder & Lumley. To facilitate comparison, their flow conditions and grid size and shape were matched as closely as possible.

The decay of turbulence behind a grid has at least two distinct regions. The first, termed the initial period, is usually considered to exist in the region between 10 and 150 mesh lengths from the grid. Within this space experiments have shown that the turbulent-energy u'^2 decay is nearly proportional to $(x-x_0)^{-1}$. Here x is the distance from the grid and x_0 is the virtual origin where, via the linear decay law, it is implied that the turbulent decay process began with infinite energy. A second region, termed the final period, is located beyond 500 mesh lengths and is characterized by a decay of turbulent energy proportional to $(x-x_0)^{-\frac{5}{4}}$. There is also some evidence that a third region exists between the first two where $u'^2 \propto (x-x_0)^{\frac{10}{7}}$. In the present study all measurements were made between 15 and 90 mesh lengths, thus located within the initial period of decay. For simplicity, a linear decay law was assumed to be applicable.

3.2. *Analysis of decay*

The obvious disadvantage of using grid turbulence in dispersion studies is the large-scale non-homogeneity in the streamwise direction of the flow. During the initial period, the turbulence intensity decays by a factor of approximately $\frac{5}{2}$ (Batchelor 1952). To account for this decrease in turbulent energy, accompanied by an increase in integral lengthscale, Taylor (1935) and later Batchelor (1952) suggested that dimensional and temporal scaling factors be invoked, adjusting the decaying field in such a way that the resulting data would approximate the characteristics of stationary turbulence. These and similar techniques have been used and proven reliable, although not always necessary, in the past (Batchelor 1952; Uberoi & Corrsin 1952; Townsend 1955; Frenzen 1963; Snyder & Lumley 1971).

Typically, grid flows are characterized, in the initial period, by self-similar spectral distributions (Steward & Townsend 1951). This was also found to be the case in the present study. It is therefore reasonable to approach the problem of decaying turbulence along the particle trajectory as being quasi-stationary, especially over the relatively small diffusion times used in this set of experiments (e.g. from $x/M = 20$ to $x/M = 70$). As pointed out by Nir & Pismen (1979), the assumption of quasi-stationarity is valid if the particle time constant τ_p is small compared with the representative decay time of the turbulent intensity. Following Nir & Pismen the decay time perceived by a particle suspended in the decaying turbulent field having a streamwise velocity $\bar{U}$ can be estimated as

$$ t_r^{-1} = \bar{U} \frac{\mathrm{d}\ln(u')}{\mathrm{d}(x-x_0)}. \tag{6} $$

In the most extreme case, the lowest value of t_r, for the experimental conditions selected in the present study, was 0.15, which is at least one order of magnitude larger than the largest particle time constant (table 1). It would seem therefore that the assumption of quasi-stationarity along a particle trajectory is justified. In addition,

Parameter	5 µm glass sphere	57 µm glass sphere
Diameter (µm)	5	57
Density (kg/m^3)	2475	2420
τ_p (ms)	0.192	24.4
τ_p/τ_k†	2.34×10^{-2}	2.972
q_p (C)‡	1.66×10^{-15}	9.71×10^{-14}
Stokes velocity (cm/s)	0.188	23.26
Terminal velocity (cm/s)	0.188	23.16
Reynolds number	6.30×10^{-3}	0.887

† $\tau_k = 8.21 \times 10^{-3}$ s at $x/M = 45$.   ‡ q_p, measured particle charge.

TABLE 1. Particle data

it will be shown below that the particle mean-square dispersion measurements made between $x/M = 20$ and $x/M = 70$ were found to be very nearly linear with distance from the grid suggesting further evidence of the validity of the quasi-stationary assumption.

3.3. *Choice of particles*

The particles used in this study were selected with reference to particle inertial effects on the basis of the particle relaxation time

$$\tau_p = \frac{d_p(2\rho_p/\rho_f - 1)}{36\nu}, \tag{7}$$

where ρ_p and ρ_f are the particle and fluid densities respectively and ν is the kinematic viscosity of the fluid. Since the crossing-trajectory effects could be controlled by adjustments made in the electric field, the only advantage of selecting particles having different relaxation times was to observe the effect of particle inertia.

The particles used were selected on the basis of the above considerations balanced with regard to availability, low cost, sphericity, and the ability to be accurately sorted into narrow-size distributions. The two particles chosen were 5 µm solid glass beads from Potters Industries Inc. and 57 µm solid glass beads from Bellotini Corp. Both particles have a high degree of sphericity and were relatively inexpensive. The important parameters of the two particles are listed in table 1. All flow-field variables used in the table were referenced to the position $x/M = 45$ in the wind-tunnel test-section, which was nearly at the centre of the section. The terminal velocities were calculated first by assuming a linear drag law $v_d = \tau_p g$ (Stokes velocity) and also using a method applying an Oseen-type correction (Fuchs 1964). Particle Reynolds numbers were based on the latter terminal velocity.

The maximum possible charge that can be given a particle is a function of the square of the diameter. For this reason, it was crucial to have particles of a very narrow size distribution to produce particles having nearly identical charge. To determine the particle-size distributions accurately a Coulter Counter model TA particle-size analyser was used. This device counted the number of particles within predesignated size groups. The small particles were purchased directly from Potters with a distribution of approximately 5 µm ± 1 µm (figure 1).

The large particles were first sorted using an Alpine American Corporation model A100 MZR zigzag particle classifier to provide a size distribution of 57 µm ± 6 µm (figure 2). The upper and lower limits of the distributions presented are set by the
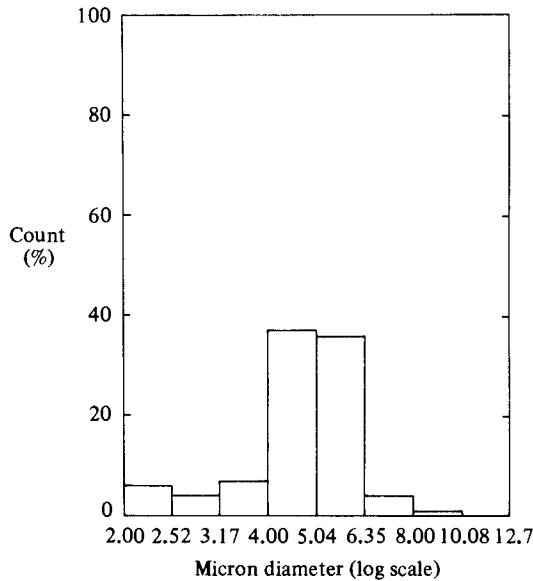
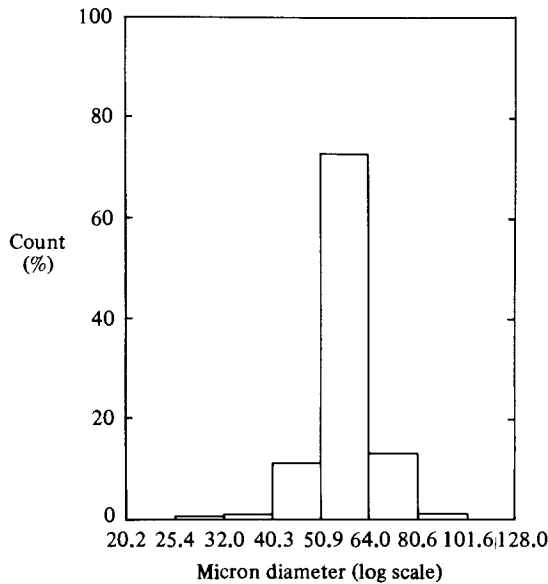FIGURE 1. 5 μm particle-size distribution.

FIGURE 2. 57 μm particle-size distribution.

predesignated groups of the Coulter Counter particle analyser. It is possible, in fact very likely in the case of the large particles, that the actual size distribution was narrower than that reported by the analyser.

3.4. *Particle charging and feeding system*

The particle charging and feeding mechanism is shown in figure 3. It consists of a fluidized-bed particle injector and a small wire-and-plate type particle-charging section with a 10 kV high-voltage power supply. The fluidized-bed particle feeder consisted of a cylindrical tube, 60 cm long and 5 cm in diameter. Attached to the
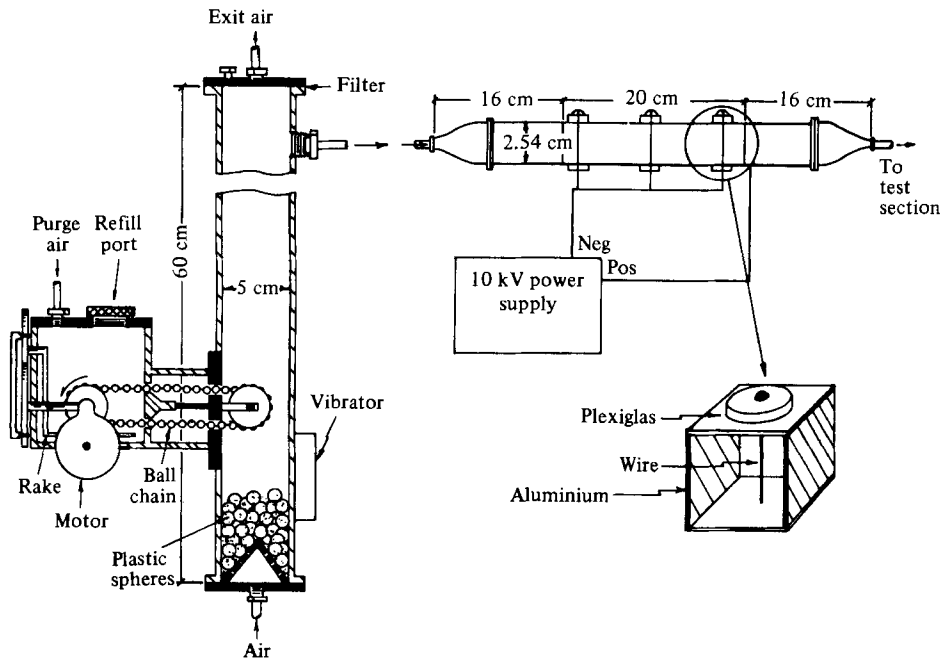
FIGURE 3. Particle charging and feeding system.

side of the cylinder was a particle reservoir equipped with a variable-speed bead chain feeding device and a rake to prevent particles from packing within the feeder. In all, six parameters controlled the particle-feeding process. These were the fluidized bed pressure, air-flow rate, reservoir pressure, bead chain drive speed, and two air-control valves, one on top and one leading to the charger. By careful manipulation of these parameters, the particle-seeding density could be selected and maintained for adequate periods of time to obtain concentration measurements.

The particle-charging section consisted of a 2.54 cm square channel having sides made of aluminium plates and a top and bottom made from Plexiglas. Three 0.05 mm diameter steel wires were stretched between the plates at 5 cm intervals. The particle charger established a corona discharge from the wires producing an ion flux, thereby charging the particles. An estimation of the minimum voltage required to produce a corona discharge in a wire-and-plate precipitator-type particle charger is given by (Moore 1973)

$$V_c = r_0 E_c \ln\frac{d}{r_0}, \tag{8}$$

where r_0 is the wire radius and d, for the particular geometry used, is given by $d = 4s/\pi$, where s is the wire-to-plate spacing. The critical electric field E_c may be calculated from the empirical equation (Moore 1973)

$$E_c = 32.2 \times 10^5 + 8.846 \times 10^4 (r_0 \delta)^{-1}, \tag{9}$$

where δ is the relative density of air, assumed equal to 1. Substituting into the above equations gave an estimate of voltage necessary to produce a corona discharge of $V_c = 6.7$ kV. Values for V_c obtained through the above analysis are usually high. When testing the charger the hissing sound and the ozone odour characteristic of a negative corona were present at about 5 kV. Also, sparkover occurred at about 13 kV. To produce the highest charge possible on the particles, the operating voltage was set and maintained at 8.84 kV. This value was sufficient to charge the particles without sparkover at normal seeding rates.
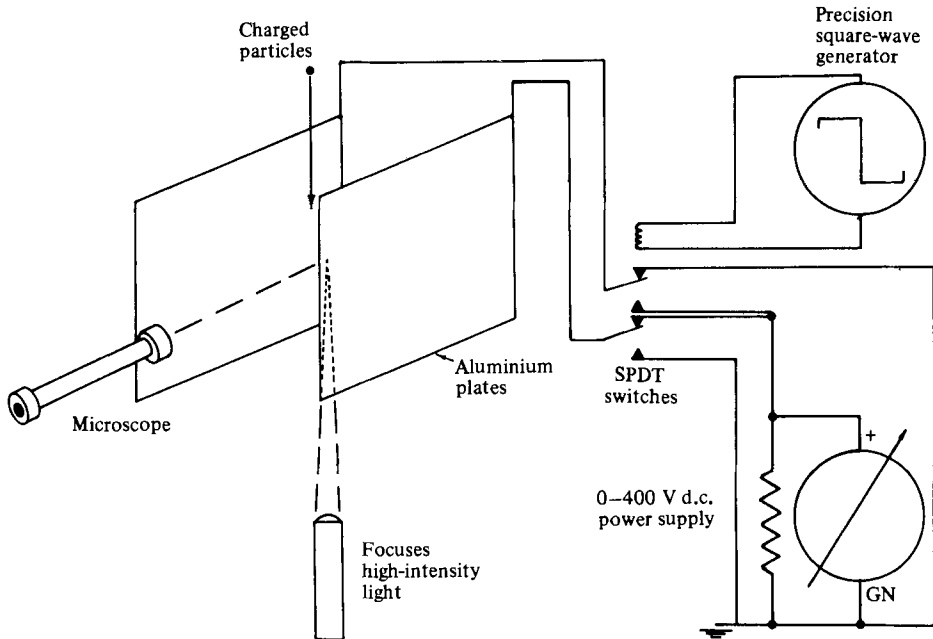
FIGURE 4. 5 μm particle-charge detector.

The saturation charge of a nonconducting particle is written in terms of the particle diameter, relative dielectric constant ϵ, the charging electric field E_{ch}, and the permeability of free space ϵ_0 as

$$q_p = \frac{9\pi\epsilon\epsilon_0 \, E_{ch} \, d_p^2}{2+\epsilon}. \tag{10}$$

The diameter of the smallest particle was nominally 5 μm so the effect of diffusion charging, usually important for particles of diameter less than 0.2 μm, was negligible and field charging was the dominate mechanism. From (10), using (9) to estimate the charging electric field, the particle charges are calculated to be 7.8×10^{-15} C for the 5 μm particle and 8.8×10^{-13} C for the 57 μm particle. Comparison between these calculated charges and the measured particle charges (table 1) is remarkably close considering the method used to estimate the charging electric field.

Measurements of particle charge were made using two devices, one for each particle size. For the 5 μm particles a modified Millikan apparatus was constructed (figure 4). This apparatus consisted of a small Plexiglas chamber holding two aluminium plates. The aluminium plates were connected to a 400 V d.c. power supply through two SPDT switches. The switches were triggered by a precision square-wave generator which continually reversed the polarity of the plates. A focused high-intensity light beam was directed to the centre of the chamber to illuminate the particles. The reflected light allowed the use of a low-power microscope with a wide field of view. Although the particles were smaller than the resolution limit of the microscope, reflected light could easily be seen.

Particle charge was measured by allowing particles to fall between the plates, causing them to oscillate back and forth while being observed through the microscope. By adjusting the voltage of power supply the particles could be made to traverse a calibrated distance, as seen by the use of grid lines inside the microscope. With the voltage known the particle charge could easily be deduced (Wells 1982). Figure 5 shows the charge distribution observed for 50 of the 5 μm particles.

The free-fall velocity of the 57 μm particles is too high to allow particle-charge tests
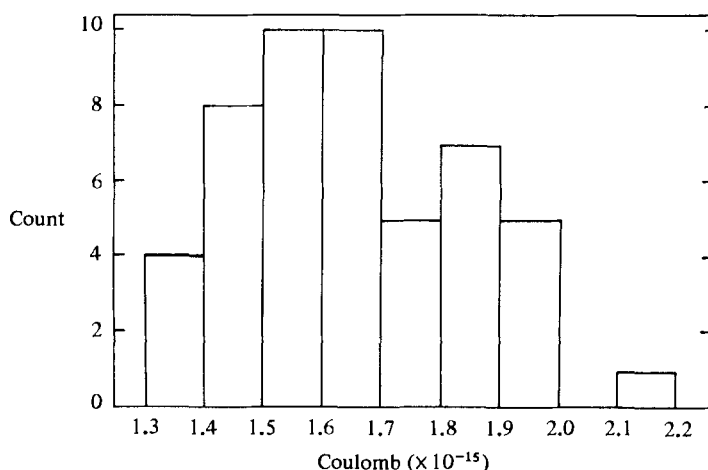
FIGURE 5. 5 μm particle-charge distribution.
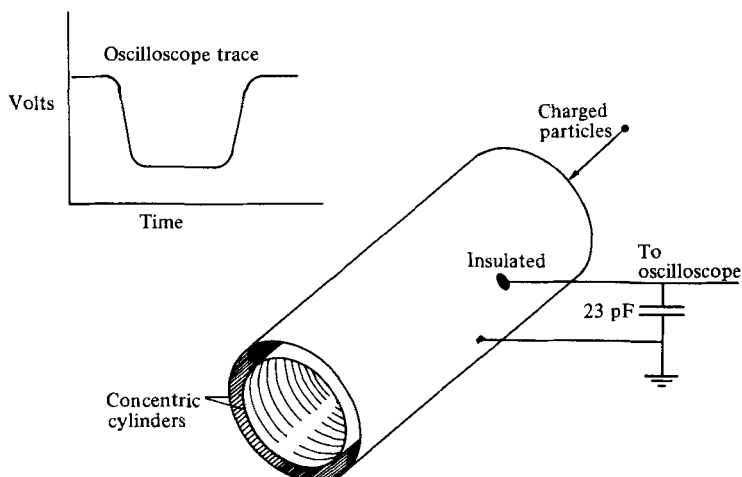
FIGURE 6. 57 μm particle-charge detector.

to be conducted using the Millikan device described above. To test the charge of these larger particles the device shown in figure 6 was designed. This device consisted of two concentric cylinders connected by a 23 pF capacitor. When a charged particle passed through the inner cylinder a voltage jump could be measured on the oscilloscope. The particle charge was then equal to the total capacitance divided by the measured output voltage, shown in the insert (figure 6). This device could not be used for the smaller particles because the small charge of the 5 μm particles produced an undetectable voltage. The charge distribution obtained from this apparatus for 50 of the 57 μm particles is shown in figure 7. The uncertainty in the measured particle charge for the 5 μm particles was 20 %, and for the 57 μm particles was 4 % (Wells 1982). The average particle charge in each case is listed in table 1.

Upon leaving the charging section, the particles were introduced into the wind tunnel through a thin-walled 0.476 cm diameter plastic tube. It was anticipated that adhesion of the particles to the tube wall would be a problem. Calculations indicated that only surface tension due to excessive moisture in the air could cause adhesion (Wells 1982). To avoid this problem the air was first filtered before entering the
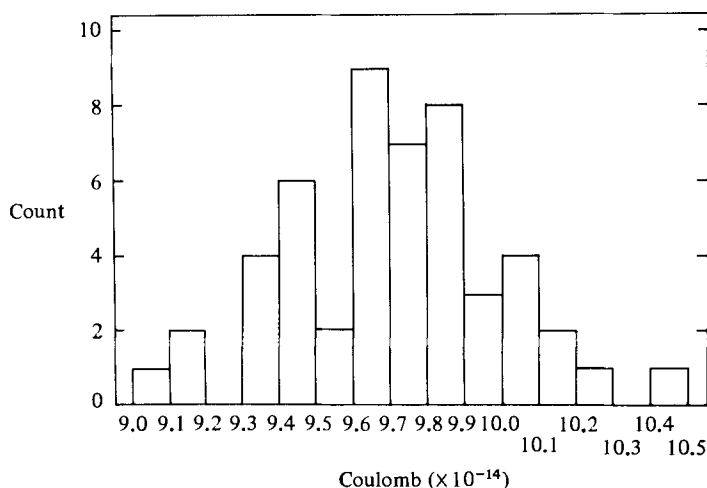
FIGURE 7. 57 μm particle-charge distribution.

particle feeding and charging system and as a result no adhesion problems were observed within the feed tube.

To estimate the contribution of the space charge to the dispersion of the charged particles, a solution to Poisson's equation was obtained (Wells 1982). The results indicate that space-charge diffusion effects may be neglected. In addition to the above calculation, particle mean-square displacement measurements were made in the test section using both charged and uncharged particles. No significant difference between the two cases could be detected. Also a flow-visualization study was conducted by reflecting a sheet of laser light vertically down the test section while releasing both charged and uncharged particles into the flow, then photographing the spread of the particles. Again no significant increase in the spread of the particles due to particle charge could be seen.

3.5. The wind tunnel

The construction of the wind tunnel is shown in figure 8. The tunnel was an axial fan type capable of producing a maximum discharge of approximately 5000 cfm. The air velocity within the tunnel was governed by a variable-resistance controller specially designed for fine resolution around the desired operation range of 6.5 m/s. Fan r.p.m. was monitored using a magnetic pickup sending voltage peaks to a Hewlett-Packard timer counter.

Air enters the wind tunnel through a large filter chamber where dust particles in the ambient air are removed. The air then passes through two contractions and a series of flow-straightening devices before entering the test section. These include two coarse-mesh screens immediately following the fan, a perforated plate with 6.35 cm diameter holes symmetrically placed to break up the large eddies, a symmetric circular-to-square-section contraction, a medium-mesh screen, a bank of 17.7 cm by 0.635 cm diameter drinking straws, a fine-mesh screen, and finally a symmetric 1.27:1 contraction just ahead of the grid. Following the test section was a honeycomb to prevent end effects and a large stagnation chamber to collect particles sent through the tunnel.

The wind-tunnel test section was composed of two glass plates 2.5 m × 0.795 cm × 35.5 cm for vertical walls, and two 2.2 m × 0.794 cm × 35.5 cm electrically isolated aluminium plates for horizontal walls. Attached to the aluminium
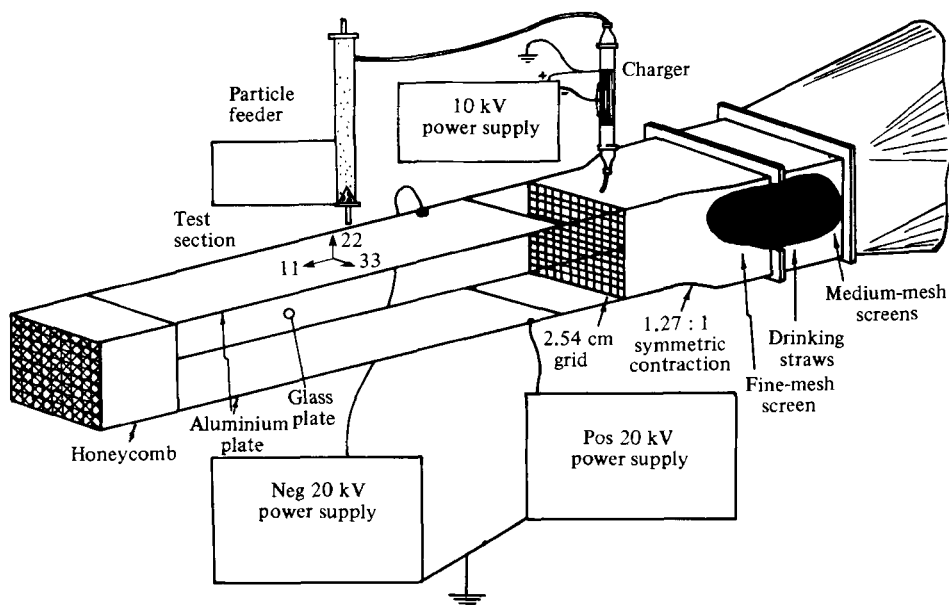
FIGURE 8. Wind-tunnel test section.

plates were two 20 kV high-voltage power supplies, one positive and one negative, capable of producing a maximum electric field intensity of about 100 V/m. The power leads from the supplies to the plates were easily removed to enable reversal of the electric field. This reversal was done, in some cases, to counteract the influence of gravity on the large particles. The output voltage from the supplies was first dropped through resistor chains, then monitored using a Keithley digital voltmeter. Two microammeters were also connected in series with the power supplies to monitor the current to the plates. The transverse dimensions of both the horizontal and vertical plates increased from 35.5 to 37.0 cm in the downstream direction to accommodate the increase in boundary-layer thickness. This variation in height caused an approximate 1 % deviation in the electric field. Mean-velocity measurements were taken while adjusting the degree of divergence of the aft portion of the test section to ensure its proper placement. The mean operating velocity was set at 6.55 m/s to match the conditions of Snyder & Lumley (1971).

The large particles had an Oseen velocity of 25.3 cm/s. Since these particles spend about 0.35 s in the test section, a minimum natural free-fall distance would be about 10 cm. Originally it was desired to at least double the 'natural' free-fall velocity using the electric field, so a 20 cm square test area down the entire length of the test section was deemed sufficient. The measured boundary-layer thickness at the end of the section was approximately 2 mm, leaving ample room for the 20 cm square test region outside the effects of the boundary layer. Subsequent measurements indicated, however, that it was possible to achieve drift velocities four times that due to gravity in the case of the 57 μm particle. When encountering drift velocities this large, it was necessary to limit measurements to the front half of the test section.

Grid selection was based on the need to generate the highest turbulence level possible and still maintain a locally isotropic field. A large grid spacing was desirable to produce high turbulence intensity, but to minimize wall effects the ratio of the test section width to the grid spacing should be greater than 10.0. Based on these considerations a 2.54 cm grid spacing was chosen. The grid was constructed of

0.476 cm square rods at 2.54 ± 0.002 54 cm intervals in a biplanar configuration. This gave a solidity ratio (projected solid area over total area) of 0.34. Square rods, rather than cylindrical rods, were chosen on the basis of evidence suggesting that they produce higher turbulence levels.

4. Fluid-turbulence measurements

The turbulent gas-flow measurements were made using a TSI model 1050 constant-temperature hot-wire anemometer system. The bulk of the measurements were made using a TSI model 1243 crosswire (X-wire) probe, while some preliminary measurements were made with a TSI model 1240 single-wire probe. The anemometer output signals were monitored using both an oscilloscope and two digital voltmeters. In addition, a TSI model 1076 digital d.c./r.m.s. voltmeter was used to monitor alternately the r.m.s. voltages from each anemometer. In series with the anemometers were two eighth-order Butterworth-type low-pass filters. The filters were set with a cut-off frequency of 1 kHz and were capable of rolling off 32 dB within 1 octave (2 kHz). Next in series were two sample-and-hold devices to allow simultaneous sampling. A DEC PDP 11/03 minicomputer was used to digitize the data, which were ultimately stored on a floppy disc for later reduction. Details of the probe calibration, data acquisition, and data processing are given by Wells (1982).

4.1. *Fluid-turbulence results*

The flow region of interest was contained in a volume 20.3 cm square by 3.05 m long, down the centre of the wind-tunnel test section. The fluid field in this region was measured to ensure it was void of any wall boundary-layer effects or any non-uniformities in the flow regime. Measurements were taken over an 81-point grid covering the 20.3 cm square area of the test section at each of the locations $x/M = 15$, $30, 45, 60, 75, 90$. The turbulence was found to be homogeneous in planes perpendicular to the mean flow. At any particular x/M-location the turbulence intensity was found to vary less than 5% over the entire 81-point test grid. A large degree of transverse homogeneity was found to exist throughout the measuring section, even at the position nearest the grid, $x/M = 15$, where some authors have reported large variations.

To indicate the degree of local isotropy, the ratio of the mean-square velocity in the streamwise direction u'^2 to that of the vertical v'^2 and horizontal w'^2 cross-stream direction was computed. Figure 9 shows typical results obtained from these calculations along a vertical plane down the centre of the test section. Throughout the test section the local isotropy, as indicated by the above parameters, was found to vary less than 5%. Finally, the probability density function $P(u/\sigma)$ of the fluctuating velocities, where $\sigma = u'$, was found to be nearly Gaussian (figure 10).

4.2. *Decay of turbulence*

Measurements of decay of the turbulent energy in the streamwise direction are compared with data found in the literature in figure 11. The figure shows that the present data compares well with that of other investigators using square bar grid construction with the possible exception of Snyder & Lumley. The data of Batchelor & Townsend (1948) and Dryden *et al.* (1937) were acquired using grids constructed of circular rods, which generally produce less turbulent energy (Corssin 1963).

Figure 12 shows both the transverse and longitudinal turbulence decay curves. Both are nearly linear, supporting the assumption that the turbulent energy decayed
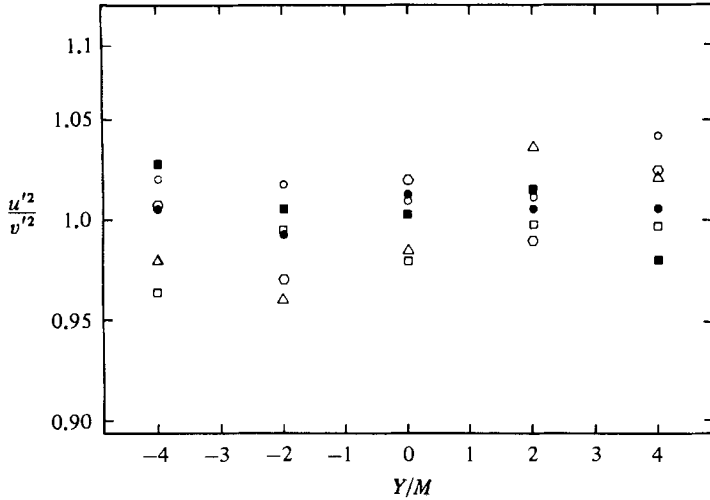
FIGURE 9. Local isotropy: $\bigcirc$, $x/M = 15$; $\square$, 30; $\triangle$, 45; $\bigcirc$, 60; $\bullet$, 75; $\blacksquare$, 90.
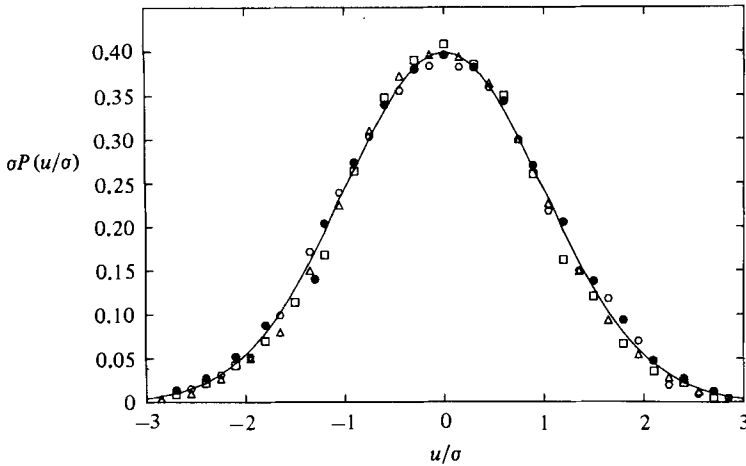

FIGURE 10. Probability density of velocity fluctuations: $\triangle$, $x/M = 15$; $\bullet$, 45; $\square$, 60; $\bigcirc$, 90.

as $(x-x_0)^{-1}$. In addition, the two curves were found to be statistically equivalent (Wells 1982). The individual energy-decay curves are given by

$$\frac{\overline{U}^2}{v'^2} = 53.224\left[\frac{x}{M} - 7.053\right], \tag{11}$$

$$\frac{\overline{U}^2}{u'^2} = 56.546\left[\frac{x}{M} - 8.867\right]. \tag{12}$$

Combining both data sets, a 'universal' decay curve was obtained as follows:

$$\frac{\overline{U}^2}{\mu'^2} = 54.88\left[\frac{x}{M} - 7.987\right], \tag{13}$$

which assumes $\mu'^2 = u'^2 = v'^2 = w'^2$. In what follows, (13) will be used whenever calculations require the use of a decay curve.

Finally, the calculated point of virtual origin of decay x_0 was examined. Figure 13 (reproduced from Naudascher & Farrell (1970) shows the variation of x_0 with R_b,
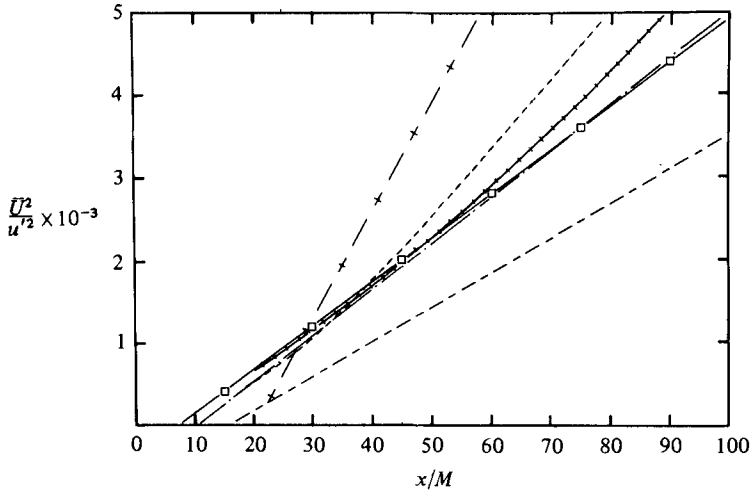
FIGURE 11. Turbulent-energy decay comparison: $+\,-$, Batchelor & Townsend (1948); $---$, Dryden *et al.* (1937); $+\,+\,+$, Compte-Bellot & Corrsin (1966); $-\cdot-$ Baines & Peterson (1951); $------$, Snyder & Lumley (1971); $\square$, present data.
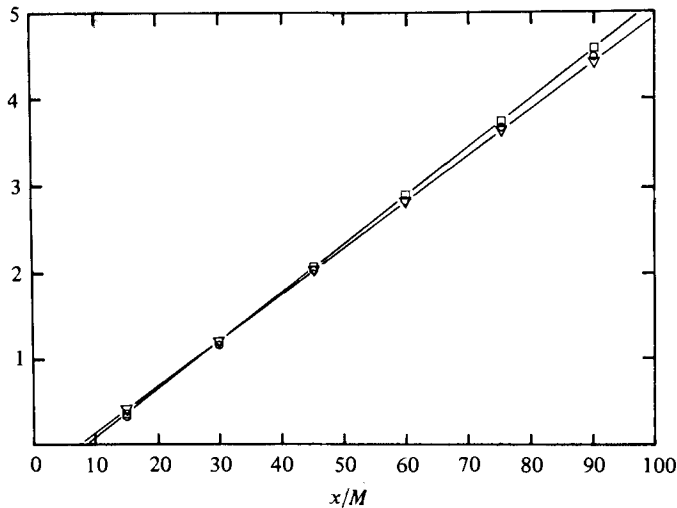
FIGURE 12. Turbulent-energy decay: $\bigtriangledown$, $U^2/u'^2 \times 10^{-3}$; $\square$, $U^2/v'^2 \times 10^{-3}$; $\bigcirc$, single hot wire.

the Reynolds number based on the grid bar width b, using data taken by several other investigators. As can be seen, the virtual origin obtained in the present study agrees very well with previous estimations. It should be noted that the value for x_0 obtained by Snyder is quite high, causing the discrepancy in the linear fit observed in figure 11.

4.3. *Autocorrelation measurements*

The autocorrelation coefficients were calculated along the centerline of the test section. Both the longitudinal $f(\tau)$ and the lateral $g(\tau)$ correlation functions were computed using

$$f(\tau) = \frac{\overline{u(0)\,u(\tau)}}{u'^2}, \tag{14}$$

$$g(\tau) = \frac{\overline{v(0)\,v(\tau)}}{v'^2}, \tag{15}$$
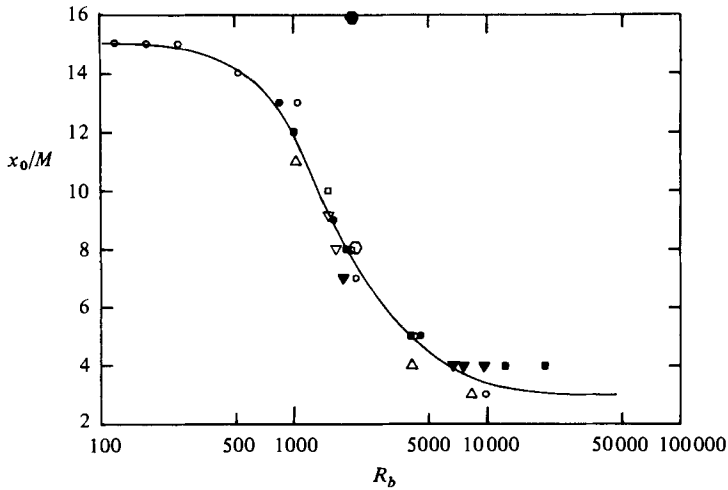
assuming local isotropy and stationarity.

FIGURE 13. Virtual-origin comparison: ○, Batchelor & Townsend (1948); ▽, Stewart & Townsend (1951); ■, Van der Hegge Zijnen (1958); □, Uberoi & Corrsin (1952); ●, Snyder & Lumley (1971); ▼, Dryden *et al.* (1937); ⬠, present data.
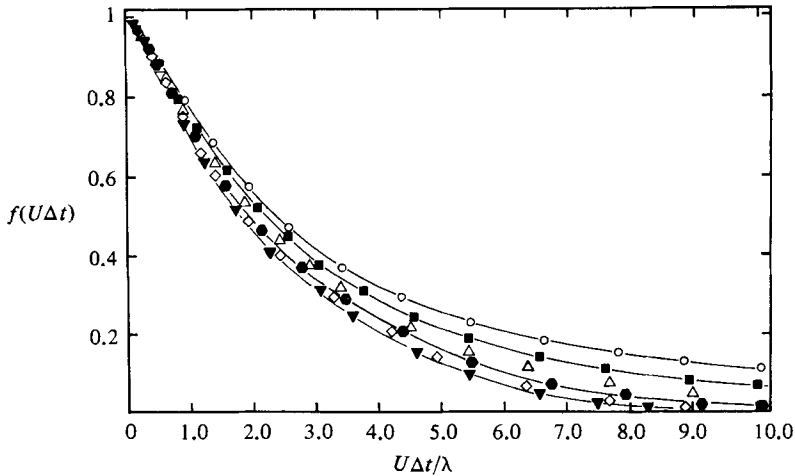
FIGURE 14. Longitudinal autocorrelation coefficients: ○, $x/M = 15$;
■, 30; △, 45; ●, 60; ◇, 75; ▼, 90.

The results on the longitudinal correlation coefficient are shown in figure 14, where $f(\tau)$ is plotted against a correlation distance $x = \bar{U}\Delta t$ non-dimensionalized by the Taylor microscale λ. A high degree of self-preservation was evident for higher frequencies.

The transverse correlation coefficients are plotted in figure 15. The point of zero-crossing, characteristics of Eulerian lateral coefficients, was found to be approximately $\bar{U}\Delta t/\lambda = 5$.

The longitudinal $T_{E_{11}}$ and transverse $T_{E_{22}}$ integral timescales were calculated from $f(t)$ and $g(t)$ respectively, using the definitions

$$T_{E_{11}} = \int_0^\infty f(\tau)\,d\tau, \tag{16}$$
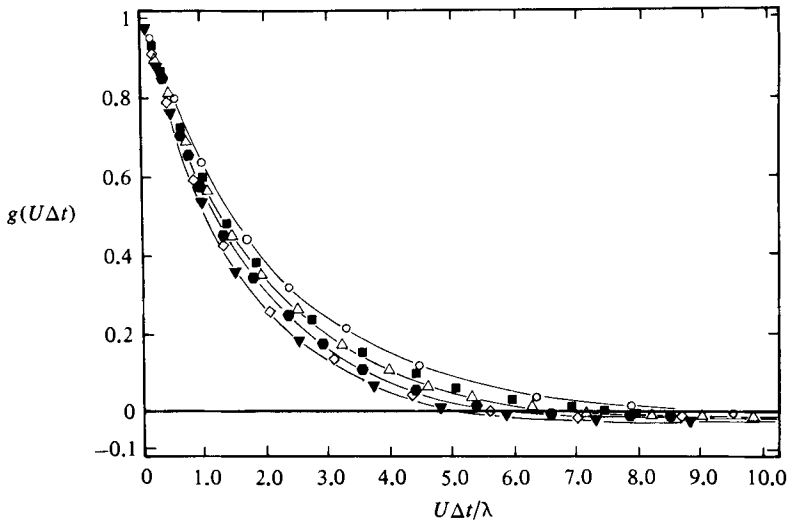
$$T_{E_{22}} = \int_0^\infty g(\tau)\,d\tau. \tag{17}$$

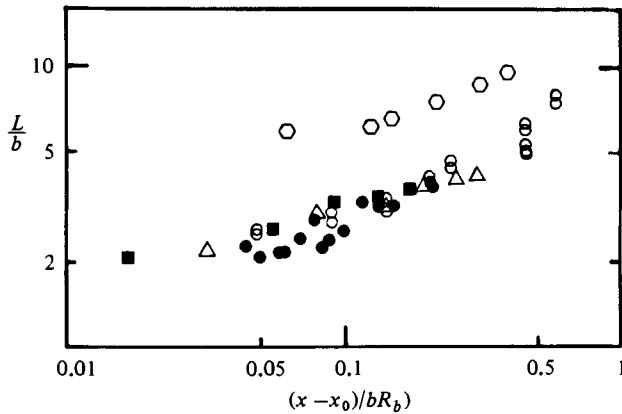FIGURE 15. Lateral autocorrelation coefficient: ○ $x/M = 15$; ■, 30; △, 45; ●, 60; ◇, 75; ▼, 90.

FIGURE 16. Longitudinal integral lengthscales: ▽, Batchelor & Townsend (1948); ○, Dryden *et al.* (1937); ●, Van der Hegge Zinjnen (1958); ○, Snyder & Lumley (1971); ■, present data.

The resulting longitudinal scales are shown in figure 16. The integral scales compare well with other investigations using similar grid Reynolds numbers, with the exception of Snyder & Lumley.

4.4. *Power spectra*

The one-dimensional power-spectral density function was computed using the Cooley–Tukey fast Fourier transform (FFT) algorithm. The normalized spectral estimates were calculated making use of the following convention:

$$u'^2 = \int_0^\infty E_{11}(k)\, \mathrm{d}k, \tag{18}$$

$$v'^2 = \int_0^\infty E_{22}(k)\, \mathrm{d}k, \tag{19}$$

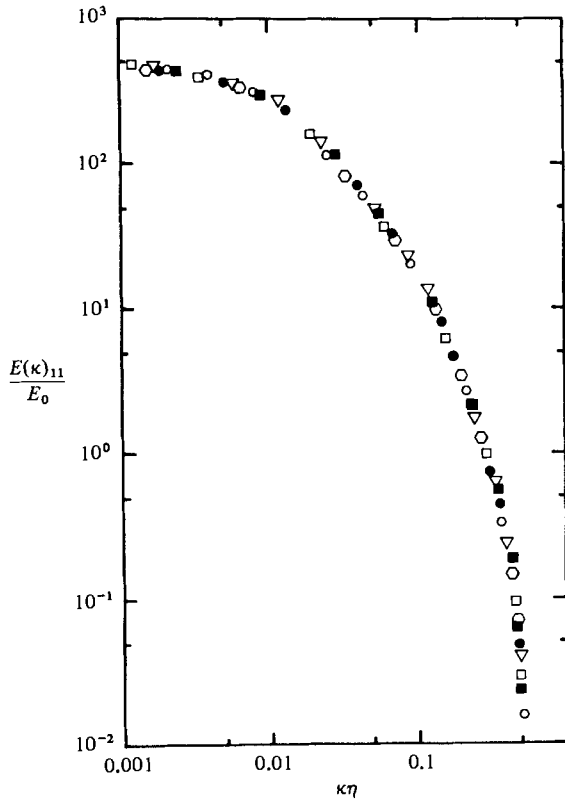where $E_{11}(k)$ and $E_{22}(k)$ are the streamwise and vertical cross-stream one-dimensional energy spectra.

FIGURE 17. Longitudinal one-dimensional energy spectrum: $\bigcirc$, $x/M = 15$;
$\square$, 30; $\ominus$, 45; $\triangledown$, 60; $\bullet$, 75; $\blacksquare$, 90.

The longitudinal and lateral power spectra plotted in Kolmogoroff coordinates are shown in figures 17 and 18 respectively. The coordinates are non-dimensionalized using $E_0 = (\epsilon\nu^5)^{\frac{1}{4}}$, $k = 2\pi f/\bar{U}$ and $\eta = (\nu^3/\epsilon)^{\frac{1}{4}}$, where ϵ and f are the turbulent eddy dissipation and frequency respectively. In the region of high wavenumber the spectral profiles were found to collapse to a single curve.

A check of the spectral estimates was made by comparing the results of two methods of calculating the eddy dissipation per unit mass. First assuming homogeneous turbulence and a constant mean velocity, the turbulent kinetic-energy equation reduces to (Hinze 1959, p. 75)

$$\frac{1}{2}\frac{d\bar{q}^2}{dt} = -\epsilon, \tag{20}$$

then making the transformation

$$\frac{d}{dt} = \bar{U}\frac{d}{dx} \tag{21}$$

gives

$$\epsilon = -\frac{\bar{U}}{2}\frac{d\bar{q}^2}{dx}. \tag{22}$$

By assuming $\bar{q}^2 = 3\mu'^2$, where $\mu'^2 = u'^2 = v'^2 = w'^2$, ϵ may be calculated by fitting $\bar{q}^2$ versus $x - x_0$ and differentiating. The dissipation may also be calculated directly from the measured spectral-energy function (Hinze 1959)

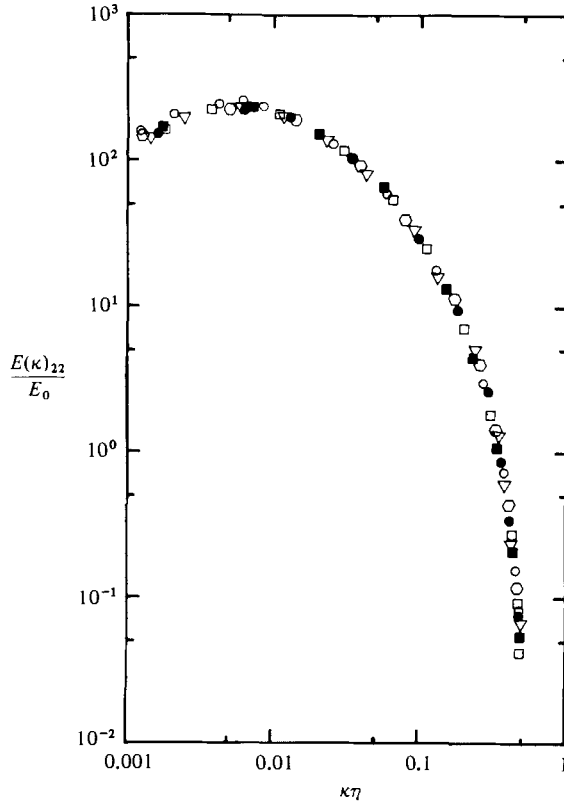$$\epsilon = 15\nu \int_0^\infty k^2 E_{11}(k)\,dk. \tag{23}$$

FIGURE 18. Lateral one-dimensional energy spectrum: $\bigcirc$, $x/M = 15$; $\square$, 30; $\square$, 45; $\bigtriangledown$, 60; $\bullet$, 75; $\blacksquare$, 90.

Calculated values of the energy dissipation using the above two methods were found to be within about 6 % of each other at every x/M-location except at $x/M = 15$. The Taylor microscale λ was calculated using the simplified form of the equation for the propagation of the correlation function developed by Kármán & Howarth (1938):

$$\frac{\mathrm{d}u'^2}{\mathrm{d}t} = 10\nu u'^2 f_0''(r). \tag{24}$$

From isotropy

$$f_0''(r) = 2g_0''(r), \tag{25}$$

then applying (21) and the definition of the Taylor microscale,

$$\frac{2}{\lambda^2} = g_0'', \tag{26}$$

gives

$$\overline{U}\frac{\mathrm{d}u'^2}{\mathrm{d}x} = \frac{-10\nu^2 u'^2}{\lambda^2}. \tag{27}$$

Assuming a linear decay of turbulence in the initial period, or $u'^2 \propto (x-x_0)^{-1}$, then substituting into (13) gives

$$u'^2 = \frac{\overline{U}^2 M}{C}(x-x_0)^{-1}, \tag{28}$$

where C is a constant obtained by fitting the experimental data. Differentiating (28) and substituting into (27) gives

$$\lambda^2 = \frac{10\nu(x-x_0)}{\overline{U}}. \tag{29}$$

x/M	15	30	45	60	75	90
$u'/\overline{U}$ (%)	4.81	2.93	2.24	1.92	1.61	1.47
$v'/\overline{U}$ (%)	4.76	2.93	2.23	1.91	1.60	1.49
T_E (ms)	1.33	1.93	2.44	2.49	2.72	2.75
λ (cm)	0.20	0.36	0.46	0.55	0.62	0.69
ϵ (cm²/s³)	61701	6247	2208	1118	673	449
η (cm)	0.015	0.015	0.035	0.041	0.047	0.052
τ_k (ms)	1.55	4.88	8.21	11.54	14.87	18.20
v_k (cm/s)	9.79	5.52	4.26	3.59	3.17	2.86

TABLE 2. Fluid-turbulence data

A similar expression for ϵ may also be obtained under the assumption of isotropy by using (Hinze 1959, p. 219)

$$\epsilon = \frac{15\nu u'^2}{\lambda^2}. \tag{30}$$

Then substituting for λ^2 from (29) and u'^2 from (28) gives

$$\epsilon = \frac{1.5\nu \overline{U}^2}{DM}\left[\frac{M}{x-x_0}\right]^2. \tag{31}$$

The values for eddy dissipation obtained from (31) were found to agree to within 10 % with those obtained from (22) and (23).

Finally, the Kolmogoroff microtime-, length-, and velocity scales were calculated from the definitions

$$\tau_k = (\nu/\epsilon)^{\frac{1}{2}}, \tag{32}$$

$$\eta = (\nu^3/\epsilon)^{\frac{1}{4}}, \tag{33}$$

$$v_k = (\nu\epsilon)^{\frac{1}{4}}, \tag{34}$$

where ϵ is obtained from (22). The results of all the turbulent gas-flow measurements are listed in table 2.

5. Particle-dispersion measurements

5.1. *LDA apparatus*

The LDA system used is shown in figure 19. The laser and optics module were fastened to a DISA 55X42 mounting bench, which sat on a large traversing mechanism. The traverse was capable of rolling the length of the test section, and could be raised and lowered a distance of 25 cm with an accuracy of ±0.0254 cm without disturbing the alignment of the PM tube. The laser was positioned horizontally so that the scattering volume remained within a vertical plane down the centre of the test section.

The LDA data-processing system is shown in figure 20. The burst signal from the processor was continually monitored on a storage oscilloscope. The digital signal from the processor was interfaced to the PDP minicomputer then stored on floppy disc for later processing.

The DISA counter processor is capable of four principal modes of operation (Buchhave 1979). Mode 2, used throughout the present study, employs a 5:8 comparator circuit combined with a period measurement based on the total number of zero-crossings. In this mode the processor outputs the Doppler period, the total
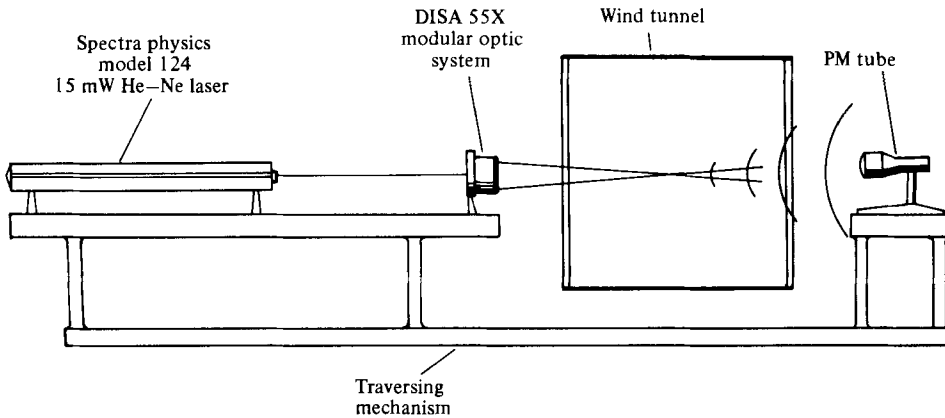
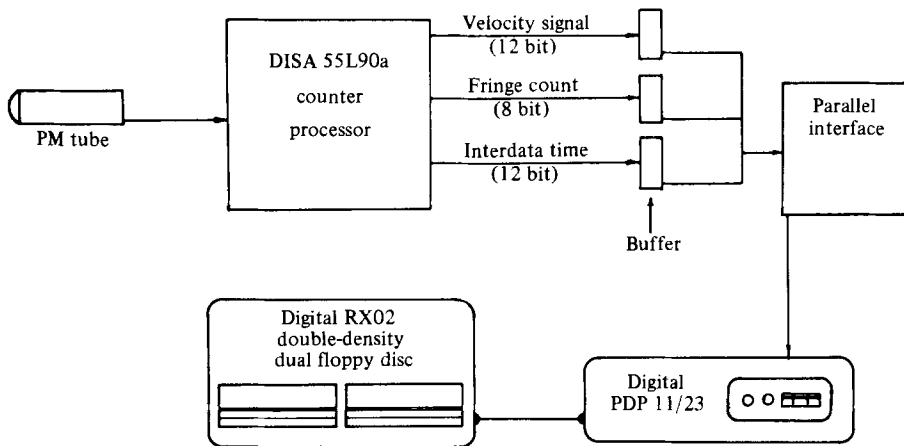FIGURE 19. Laser-Doppler anemometer system.

FIGURE 20. LDA signal-processing system.

fringe count, and the time between bursts (interdata time). Autocorrelations may then be easily calculated using the period and interdata time data while relative concentration or number density measurements are possible using the total fringe count and interdata time data.

The LDA provides velocity information averaged according to the occurrence of particles passing through the scattering volume. In a fluid containing uniformly or randomly distributed particles the probability density function of particle velocities will be biased in favour of higher velocities. This phenomenon (velocity biasing) is especially apparent in highly turbulent flows. It is possible to correct for velocity biasing by applying a weighting factor, equal to the measured residence time or the time a particle remains within the measuring volume, to the velocity estimate (Buchhave 1979). This correction was investigated, but, owing to low turbulence levels in the test section (approximately 5 % maximum), no significant improvement was realized.

5.2. *Mean and r.m.s. velocity*

Mean and r.m.s. particle-velocity measurements were made down the centre of the test section using various particle sizes d_p versus electric field E_f, configurations (i.e. drift velocity). Measurements made at higher field strengths required that the position of the measuring volume be lowered from the centreline to maintain
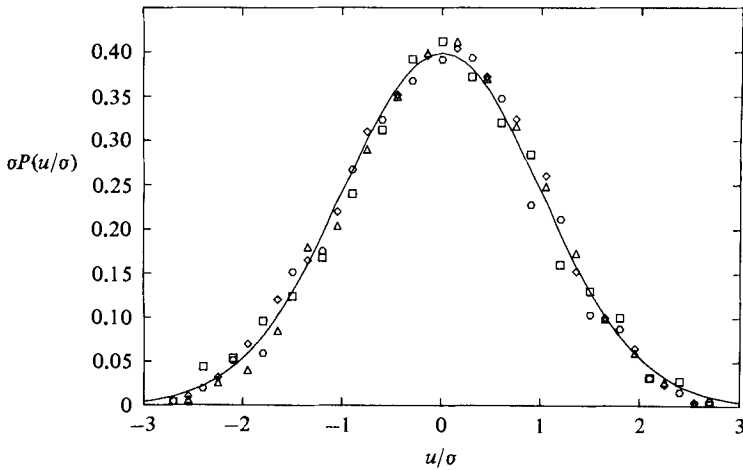
FIGURE 21. Probability density of particle-velocity fluctuations. 5 μm particles: □, $x/M = 30$; ▽, 60. 57 μm particles: ○, $x/M = 30$; ◇, 60.
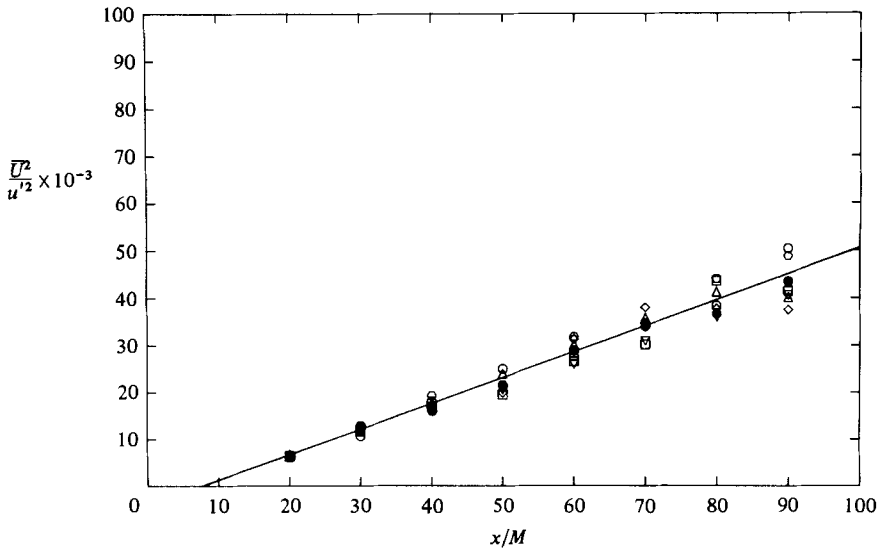

FIGURE 22. Turbulent-energy decay, 5 μm particles: ——, fluid-turbulence decay; □, $v_d = 0$; ○, 2.73; ●, 5.86; ◇, 13.31; △, 17.06; ▽, 20.91; ○, 23.65.

adequate data rates as particles were pulled toward the lower plate of the test section. Measurements were made on intervals of ten mesh lengths, beginning from $x/M = 20$. The position $x/M = 20$ was chosen as the initial position for all the LDA measurements, allowing five mesh lengths for the particle to react to the electric field and to prevent measurement errors due to electric-field end effects. Mean and r.m.s. turbulent-velocity measurements were based on averages from 6000 sample points. The average interdata time for the samples was approximately 0.01 s, or about four integral timescales, indicating a sample rate slow enough to provide statistically independent samples. In addition, mean-velocity measurements were made on vertical planes at $x/M = 2, 40, 80$ with $E_f = 0$ to ensure that a uniform velocity persisted throughout the test section with the inclusion of the particles. The measurements indicated that the presence of the particles in the test section did not alter the mean-velocity profiles.

A typical one-dimensional probability density distribution of fluctuating particle
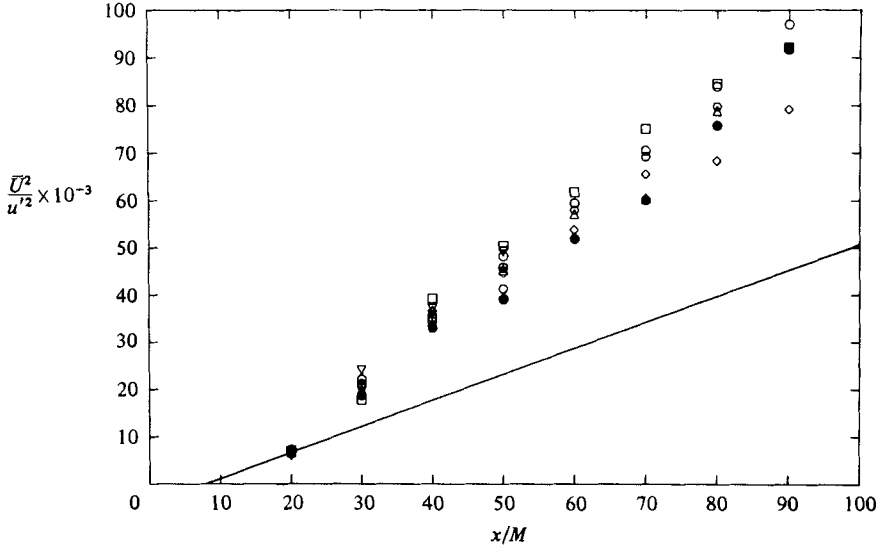
FIGURE 23. Turbulent-energy decay, 57 μm particles: ——, fluid-turbulence decay; □, $v_d = 0.0$; ○, 13.5; ●, 25.8; ◇, 39.7; △, 54.5; ▽, 81.5; ○, 108.0; ⊕, 121.6.

velocities $P(u/\sigma)$, where $\sigma = u'$, is given in figure 21. The shape of the density function closely approaches a normal Gaussian distribution.

The turbulent-energy decay curves of the 5 μm and 57 μm diameter particles are plotted against the X-wire result in figures 22 and 23 respectively. There appeared to be no significant difference in the rate of turbulence decay due solely to increases in drift velocity for a given particle size. To test this hypothesis, linear least-square curve fits were obtained for the data of each v_d for both particle size groups. Then the data within each particle size was compared at the 95 % level of significance. No significant difference existed between the turbulent-energy decay curves for the 5 μm particles. There were, however, some cases where two decay curves in the 57 μm group could not be considered equivalent at the 95 % level of significance, but no discernible trends were evident. Finally, linear curves were fit to all of the 5 μm particle decay data, then all of the 57 μm particle data, comparing each with the fluid point turbulence decay, (13). The resulting turbulent-decay equations for the 5 μm and 57 μm particle groups are respectively

$$\frac{\overline{U^2}}{u'^2} = 53.764\left[\frac{x}{M} - 7.737\right],$$ (35)

$$\frac{\overline{U^2}}{u'^2} = 121.475\left[\frac{x}{M} - 12.975\right].$$ (36)

At a 95 % level of significance the 5 μm particle turbulence decay was identical to that of the fluid. The turbulent energy of the 57 μm particle size group, however, was found to be approximately 30 % lower than that of the fluid. Also, the virtual origin estimates of both particle size groups agreed closely with the fluid measurement.

5.3. *Mean-square displacement*

Determination of particle mean squared displacement $\overline{Y^2}$ through measurement of particle concentration using LDA can present serious interpretation problems. The principal difficulty stems from the problem of accurately determining the cross-
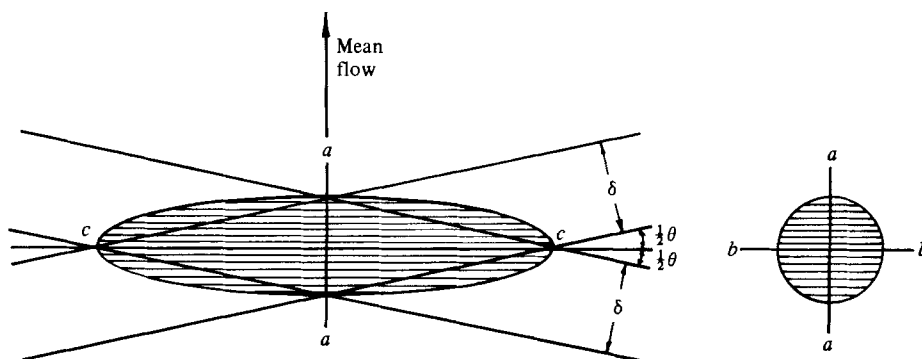
FIGURE 24. LDA measuring volume.

sectional area of the measuring volume. In addition, a further complication was observed from preliminary measurements of particle concentration which indicated that it was virtually impossible to accurately select a particular concentration level. Fortunately, determining mean-square displacement requires only the measurement of the relative number density (number of particles per unit time per unit linear displacement) rather than absolute concentration.

The LDA measuring volume is usually defined as the elliptical volume within the $1/e^2$, e $= 2.718$, boundary of the optical fringe modulation (figure 24). Since it is the vertical distribution of number density that is of interest, assuming the dispersion in the horizontal plane to be symmetric, the exposed cross-sectional area of the measuring volume is the height of the circular section a–a of the figure. The number of fringes encountered by a particle passing through this area varies from a maximum at the centre, a–a, to a minimum near the outer edges. Therefore, the number of fringes a particle crosses while passing through the measuring volume is an indication of the particle's position relative to the beam crossing point, a–a. In this manner, using mode 2 of the LDA processor, number-density measurements were made by counting the arrival of particles and measuring the number N_f of fringe crossings, then neglecting particles for which N_f was less than some reference value. The reference was somewhat arbitrary, the only requirement being that the same value be used for an entire set of mean squared displacement measurements. Generally the reference value was selected as approximately 90 % of the mean fringe count measured for the particular electric field conditions.

While it was not possible to select a given concentration, once the concentration or particle flow rate was set, that rate generally persisted or exhibited a gradual monotonic increase or decrease which was found to be linear with time. Raw number-density measurements were nondimensionalized by taking the ratio of the measured density with a value obtained at a reference position where the particle density was believed to be near maximum. This reference or centre position was frequently monitored during the measurement. If a slight deviation in the mean number density occurred during the series of measurements made between reference checks, a linear extrapolation of the data was made to account for the change.

Number-density measurements were made for the two particle sizes and various electric field strengths. Measurements were made randomly within a vertical grid, continually rechecking the arbitrary centre location to ensure that a constant efflux of particles into the test section was being maintained. The data-acquisition programme was designed to continue accepting data until 6000 points were accumulated or until 65 s had elapsed, whichever occurred first. In this manner data near

Particle diameter (mm)	Voltage V_f (V)	Electric field (V/cm)	Drift velocity (cm/s)	Uncertainty ω (cm/s)
57	−9440	−258	0	1.38
—	−4710	−127	13.5	1.41
—	0	0	25.8	1.59
—	5047	139	39.7	2.45
—	10470	287	54.5	2.55
—	20240	554	81.5	4.10
—	30040	823	108.0	5.26
—	35170	963	121.6	6.11
5	0	0	0	1.38
—	5078	139	2.73	1.38
—	10470	287	5.86	1.39
—	20240	554	13.31	1.43
—	30040	823	17.06	1.47
—	35170	963	20.91	1.52
—	39650	1086	23.65	1.53

TABLE 3. Particle drift velocity

the centre of dispersion were obtained quickly and accurately (averaged over a large number of points), while data near the edges of dispersion were gathered over long periods of time, nullifying intermittency effects. Data were continually taken at positions along the vertical grid, increasing the distance from the centre of dispersion until the number density at the edge was at least smaller than one-tenth the maximum. To account for small fluctuations in particle concentration, data were acquired a minimum of four times at each of the vertical points before moving to a new x/M-location. Repeatability was good between measurements of any given run and measurements repeated after several days. Relative number-density measurements made at different times consistently varied by less than 10%.

To reduce the data, the averaged number density at each vertical location was first divided by that of the arbitrary centre location. The relative number-density distributions were then fitted to a Gaussian distribution function by taking the logarithm of the distribution function and solving for the mean and standard deviation using a nonlinear least-squares iteration technique. The computed standard errors for the mean and standard-deviation estimates were 4% and 3–7% respectively.

The mean value for the dispersion obtained from the nonlinear fit was used as an accurate measure of the displacement of the centre of dispersion. Knowing this distance, the distance from the particle source and the mean velocity, accurate estimates of the particle's drift velocity could be obtained. Table 3 lists the electric field drift velocity relationships for each of the particle size/electric field combinations.

In the case of the 57 μm particles, it was possible to produce a drift velocity more than four times that of the natural free-fall velocity by applying the electric field. The maximum drift velocity of the 5 μm particles was approximately 25 cm/s.

Drift velocities measured in this manner agreed well with calculation based on the measured particle charge. In addition, the measured natural free-fall velocity of the 57 μm particle agrees very well with the calculated Oseen terminal velocity (table 1). The natural free-fall velocity of the 5 μm particle was too small with respect to the
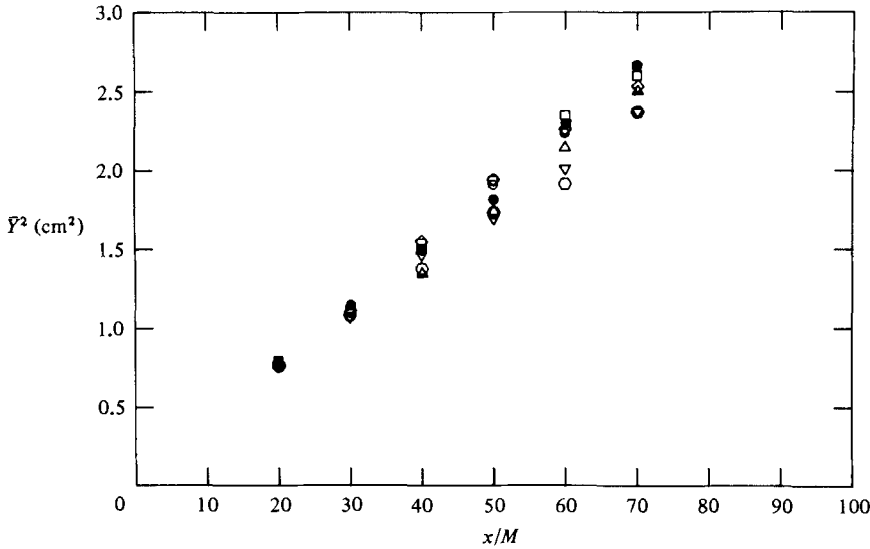
FIGURE 25. Particle mean-square displacement, 5 μm particles: □, $V_d = 0$; ○, 2.73; ●, 5.86; ◇, 13.31; △, 17.06; ▽, 20.91; ○, 23.65.
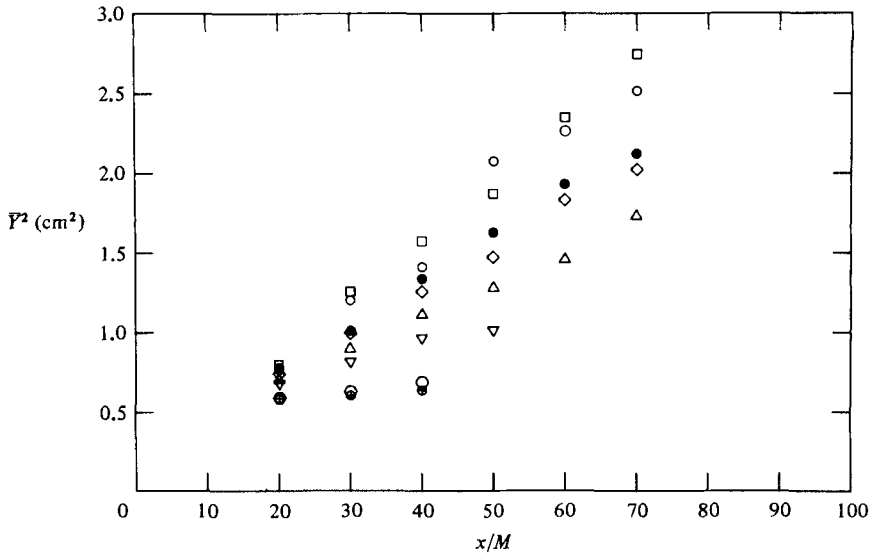
FIGURE 26. Particle mean-square displacement, 57 μm particles: □, $V_d = 0$; ○, 13.5; ●, 25.8; ◇, 39.7; △, 54.5; ▽, 81.5; ○, 108.0; ⊕, 121.6.

experimental uncertainties to detect. To obtain drift velocities less than the natural free-fall velocity, in the case of the 57 μm particles, the polarity of the electric field was reversed. The point $v_d = 0$ was found by trial and error.

The mean-squared displacement $\overline{Y^2}$ data for the 5 μm and the 57 μm particles obtained from the nonlinear fits are shown in figures 25 and 26 respectively. Linear curves were fitted through the $\overline{Y^2}$ data for each value of v_d. The slopes of these curves were then used to calculate dispersion coefficients. Attempts to fit higher-order curves were made but analysis of variance tests on the nonlinear parameters revealed them to be statistically insignificant in every case.
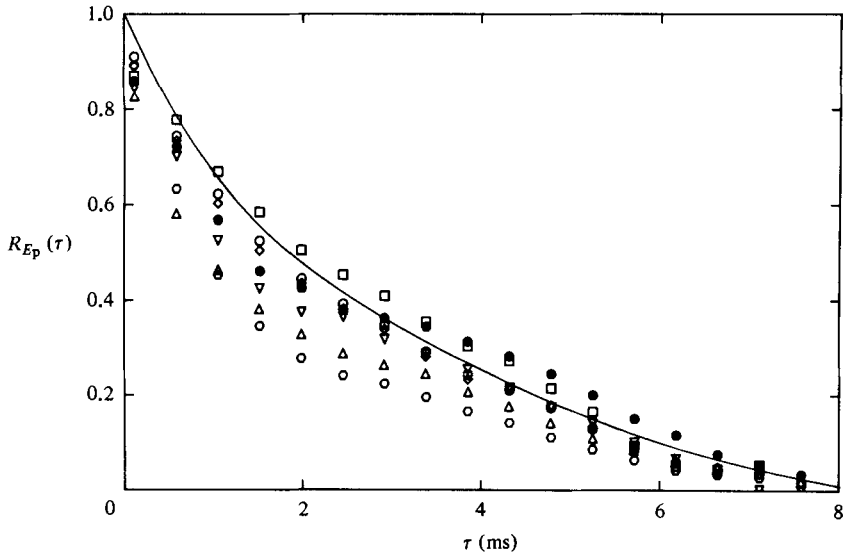
FIGURE 27. Longitudinal autocorrelation coefficient, 5 μm particles: □, $V_d = 0$; ○, 2.73; ●, 5.86; ◇, 13.31; △, 17.06; ▽, 20.91; ⊙, 23.65.
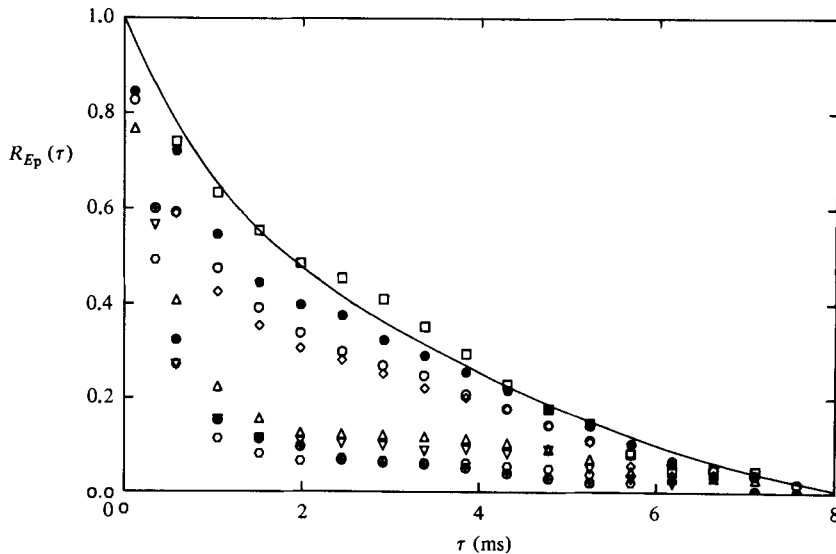
FIGURE 28. Longitudinal autocorrelation coefficient, 57 μm particles: □, $V_d = 0$; ○, 13.5; ●, 25.8; ◇, 39.7; △, 54.5; ▽, 81.5; ⊙, 108.0; ⊕, 121.6.

5.4. *Autocorrelation estimates*

Autocorrelation estimates were obtained at the position $x/M = 45$ for each of the conditions listed in table 3. It was difficult to seed heavily enough to obtain good resolution for short correlation times when using the 57 μm particles. In such cases an exponential curve was fitted to the correlation curve in the small-correlation-time region to improve the accuracy of the calculated integral scales.

Since the particle-velocity information was acquired randomly in time as particles passed through the control volume, it was necessary to first group the individual occurrences into buckets covering predesignated time intervals (Buchhave 1979). The

5 µm particles		57 µm particles	
V_d (cm/s)	T_E (ms)	V_d (cm/s)	T_E (ms)
0	2.39	0	2.41
2.73	2.26	13.5	1.82
5.86	2.11	25.8	2.09
13.31	2.21	39.7	1.72
17.06	1.79	54.5	1.05
20.91	1.94	81.2	0.97
23.65	1.63	108.0	0.49
		121.6	0.45

TABLE 4. Eulerian integral scale

size of the buckets was selected such that each would cover approximately $\frac{1}{100}$ of the measured fluid integral timescale. Correlation coefficients were then averaged within each bucket, then calculated over a total correlation time interval slightly greater than three fluid integral timescales.

The results of the correlation estimates are presented in figures 27 and 28 for the 5 µm and 57 µm particles respectively, and the corresponding integral scales are presented in table 4.

The effect of increasing the drift velocity was to decrease the correlation time. This is a consequence of a particle crossing the trajectories of fluid points and thus losing correlation more rapidly. In addition, the particle correlation curves (for the cases where the particle drift velocities were zero) appeared above the fluid point correlation curve.

5.5. Dispersion coefficients from $\overline{Y^2}$ measurements

The dispersion coefficients $D_{p22}(t)$ were calculated from the mean squared displacement data, using (1), assuming a linear increase in $\overline{Y^2}$. Dispersion coefficients obtained from the $\overline{Y^2}$ data are shown in figure 29. A definite inverse relationship exists between the particle drift velocity and the dispersion coefficient. The dispersion coefficient was found to decrease approximately as the drift velocity squared within the range of velocities tested.

5.6. Dispersion coefficients from autocorrelation estimates

The particle-dispersion coefficients were also calculated from the Eulerian autocorrelations using (1). To accomplish this, it was necessary to relate the Lagrangian and Eulerian integral timescales. It has been suggested by many authors that the Lagrangian and Eulerian correlations have similar shapes and differ only by their scales (Csanady 1963; Saffman 1962) (i.e. $R_L(\tau) = R_E(\beta\tau)$, where $\beta = T_L/T_E$. Using 'Corrsin's (1962) conjecture' and assuming a stationary turbulent field, Saffman (1962) developed an approximate relation between the Lagrangian and Eulerian timescales of fluid points which was a function of the fluid turbulence ($\beta = 0.8\overline{U}/u'$). Saffman, however, pointed out that there is no reason for this expression to be valid for grid flows, since Corrsin's closure method does not apply to decaying turbulent fields. Pasquill (1962) suggests that for atmospheric turbulence β is independent of the turbulent field, and proposes a value of $\beta = 4$, based on experimental evidence. From Saffman's relation it would then appear that β should be higher for grid flows owing to their lower turbulence intensity. Snyder & Lumley (1971) calculated $\beta = 3$
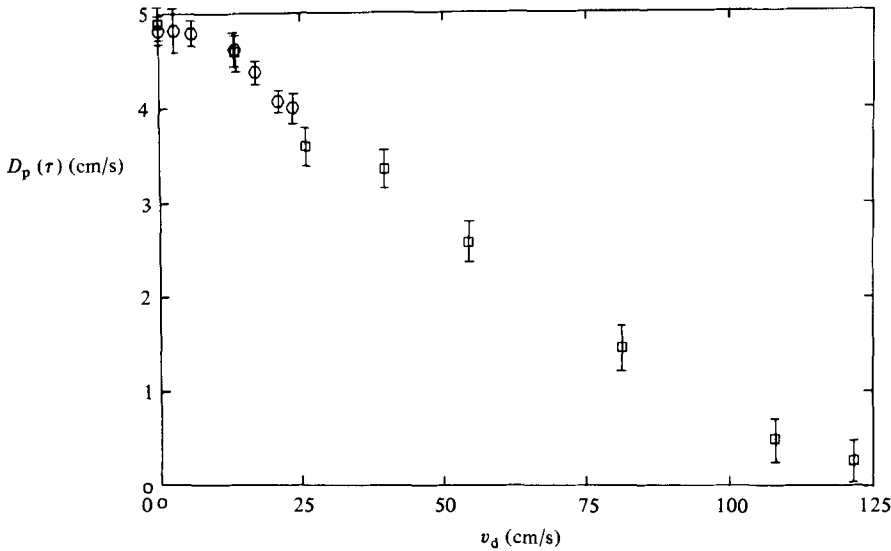
FIGURE 29. Particle-dispersion coefficients from $\overline{Y^2}$ measurements:
□, 57 μm particles; ○, 5 μm particles.

by interpreting their heavy-particle correlations as representative of Eulerian correlations and their light-particle results as representative of Lagrangian correlations. However, by comparing the Eulerian timescale resulting from Snyder & Lumley's X-wire measurements (measured at the midpoint of their test section) with their light-particle Lagrangian timescale, a value of $\beta = 22$ is obtained.

In order to compare dispersion coefficients calculated from the mean-square displacement measurements with those calculated from the autocorrelation estimates, values of β were chosen for each particle size such that the dispersion coefficients approximately matched at $v_d = 0$. The values for β obtained in this manner were $\beta = 8.2$ for the 5 μm particles, and $\beta = 15.6$ for the 57 μm particles. It was found that the ratio of the two values obtained for β using the 5 μm and 57 μm particles corresponded very closely (within approximately 1 %) to the ratio of their respective mean-square velocities (which is not surprising considering the manner in which the β-values were obtained). A similar calculation was performed with Snyder & Lumley's data, using β-values obtained by comparing the Lagrangian timescales corresponding to their largest and smallest particle sizes with the Eulerian timescale from their X-wire measurement. Again it was found that the ratio of the two values of β corresponding to the two particle sizes was nearly equal to the ratio of their respective mean square velocities (within approximately 2 %). Although there is no theoretical reason for this result, it is at least a fortunate discovery lending some justification to the method used to obtain dispersion coefficients using the Eulerian timescale measurements.

The resulting dispersion coefficients are shown in figure 30, where the solid line is a fitted curve through the data of figure 29. Although there was somewhat more scatter evident in the calculations derived from the autocorrelations, the agreement was good.

In figure 31 the results of the present study are compared to the experimental results of Snyder & Lumley by fitting their $\overline{Y^2}$ data to linear curves, then differentiating. Although some curvature was present in their $\overline{Y^2}$ estimates, as a first approximation this method facilitated comparison. The figure shows that the results
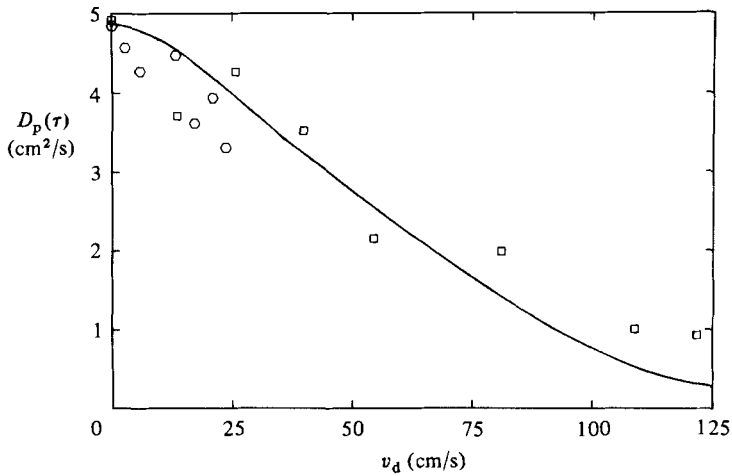
3

FIGURE 30. Particle-dispersion coefficients from autocorrelation estimates: □, 57 μm particles; ○, 5 μm particles; ———, curve fit of data from figure 29.
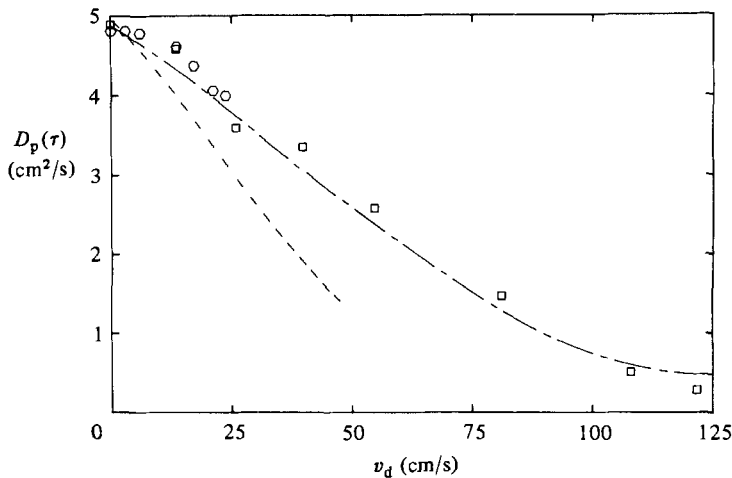

FIGURE 31. Particle dispersion-coefficient comparison: □, 57 μm particles; ○, 5 μm particles; ———, Csanady (1963); ———, Snyder & Lumley (1971).

from their data lie considerably below the present data owing to the different fluid reference location. Csanady's equation, (5), was also plotted by assuming that the fluid point dispersion coefficient was approximately equal to that of the 5 μm particle, and using Saffman's (1974) formulation relating the Lagrangian and Eulerian integral scales.

6. Conclusions

The effect of crossing trajectories decreased the long-time particle-dispersion coefficient. This decrease was made evident by a decrease in particle mean-square displacement and a decrease in the particle autocorrelation time. Crossing-trajectory effects appear to be negligible when the drift velocity is less than the r.m.s. fluid velocity, a finding consistent with Reeks (1977). A drift velocity just equal to the r.m.s. velocity would reduce the dispersion coefficient by approximately 10%.

Dispersion coefficients obtained from the mean-square displacement measurements exhibited the same trends as those obtained from the autocorrelation measurements. In the latter case, however, there was slightly more scatter due to errors involved in the correlation measurement and a probable non-uniformity in particle charge due to higher particle flow rates.

Particle inertia effects decreased the particle r.m.s. fluctuating velocity. The 57 µm particle, having a ratio $\tau_p/\tau_k = 2.972$, at $x/M = 45$, had a mean-square velocity of approximately 30 % less than that of the fluid, while the 5 µm particle, having a ratio of $\tau_p/\tau_k = 0.023$, had the same mean-square velocity as the fluid. There is some evidence that the effect of particle inertia, when isolated from the effect of crossing trajectories, is to increase the particle-dispersion coefficient. In the present case, however, this trend was small and masked by the experimental uncertainty.

REFERENCES

BATCHELOR, G. K. 1952 Diffusion in a field of homogeneous turbulence, part II, the relative motion of particles. *Proc. Camb. Phil. Soc.* **48**, 345–362.

BATCHELOR, G. K. & TOWNSEND, A. A. 1948 Decay of isotropic turbulence in the initial period. *Proc. R. Soc. Lond.* A, **193**, 539–558.

BERLEMONT, A. & GOUESBET, G. 1981 Prediction of the behavior of a cloud of discrete particles released in a fully developed turbulent pipe flow, using a non-discrete dispersion approach. In *Proc. 2nd Intl Conf. on Numerical Methods in Laminar and Turbulent Flow, Venice, Italy*, 13–16 *July*, 1981.

BUCHHAVE, P. 1979 The measurement of turbulence with the burst-type laser Doppler anemometer – errors and correction methods. PhD dissertation, State University of New York, Buffalo.

CALABRESE, R. V. & MIDDLEMAN, S. 1979 The dispersion of discrete particles in a turbulent fluid field. *AIChE J.* **25**, 1025–1035.

CHAO, B. T. 1965 Turbulent transport behavior of small particles in dilute suspensions. *Ostereichisches Ingenieur-Archiv.*, Sonderabdruck aus Bd. 18, Heft 1 und 2, p. 7.

COMPTE-BELLOT, G. & CORRSIN, S. 1966 The use of a contraction to improve the isotropy of grid-generated turbulence. *J. Fluid Mech.* **25**, 657–682.

CORRSIN, S. 1962 Theory of turbulent dispersion. In *Proc. Turbulent Diffusion Conf. Marseille, France*, pp. 27–52.

CORRSIN, S. 1963 Turbulence: experimental methods. In *Handbuch der Physik*, vol. 812, pp. 115–145. Springer.

CSANADY, G. T. 1963 Turbulent diffusion of heavy particles in the atmosphere. *J. Atmos. Sci.* **20**, 201–208.

CSANADY, G. T. 1964 An atmospheric dust fall experiment. *J. Atmos. Sci.* **21**, 222–225.

DRYDEN, H. L., SCHUBAUER, G. B., MOCK, W. C. & SKRAMSTAD, H. K. 1937 Measurements of the intensity and scale of wind tunnel turbulence and their relation to the critical Reynolds number of spheres. *NACA Reprint* no. 581.

FRENZEN, P. 1963 A laboratory investigation of the Lagrangian autocorrelation function in a stratified fluid. *Argonne Natl Lab* ANL-6794.

FUCHS, N. A. 1964 *The Mechanics of Aerosols*. Macmillan.

HINZE, J. O. 1959 *Turbulence*. McGraw-Hill.

KÁRMÁN, T. VON & HOWARTH, L. 1938 On the statistical theory of isotropic turbulence. *Proc. R. Soc. Lond.* A **164**, 192–215.

KOLMOGOROFF, A. N. 1941 Dissipation of energy in locally isotropic turbulence. *C.R. Acad. Sci. URSS* **32**, 16–18.

MEEK, C. C. & JONES, B. G. 1973 Studies of the behavior of heavy particles in a turbulent fluid flow. *J. Atmos. Sci.* **30**, 239–241.

MOORE, A. D. 1973 *Electrostatics and Its Applications*, chap. 9, pp. 194–197. Wiley.

NAUDASCHER, E. & FARRELL, C. 1970 Unified analysis of grid turbulence. *J. Engng Mech. Div. ASCE* **96** (EM2), 121–141.

NIR, A. & PISMEN, L. M. 1979 The effect of a steady drift on the dispersion of a particle in turbulent fluid. *J. Fluid Mech.* **94**, 369–381.

PASQUILL, F. 1962 *Atmospheric Diffusion*. Von Nostrand.

PISMEN, L. M. & NIR, A. 1978 On the motion of suspended particles in stationary homogeneous turbulence. *J. Fluid Mech.* **84**, 193–206.

REEKS, M. W. 1977 On the dispersion of small particles suspended in an isotropic turbulent field. *J. Fluid Mech.* **83**, 529–546.

RILEY, J. J. & PATTERSON, G. S. 1974 Diffusion experiments with numerically integrated isotropic turbulence. *Phys. Fluids* **17**, 292–297.

SAFFMAN, P. G. 1962 An approximate calculation of the Lagrangian autocorrelation coefficient for stationary homogeneous turbulence. *Appl. Sci. Res.* **11A**, 245–255.

SNYDER, W. H. & LUMLEY, J. L. Some measurements of particle velocity autocorrelation functions in a turbulent flow. *J. Fluid Mech.* **48**, 41–71.

TAYLOR, G. I. 1921 Diffusion by continuous movements. *Proc. R. Soc. Lond.* A **151**, 421–478.

TAYLOR, G. I. 1935 Statistical theory of turbulence. *Proc. R. Soc. Lond.* A **151**, 421–478.

UBEROI, M. S. & CORRSIN, S. 1952 Diffusion of heat from a line source in isotropic turbulence. *NACA Rep.* 1142.

VAN DER HEGGE ZIJNEN 1958 Measurements of the intensity, integral scale and microscale of turbulence downstream of three grids in a stream of air. *Appl. Sci. Res.* **7A**, 149–174.

WELLS, M. R. 1982 The effects of crossing trajectories on the diffusion of particles in a turbulent flow. PhD thesis, Washington State University.

YUDINE, M. I. 1959 Physical considerations on heavy-particle diffusion. In *Atmospheric Diffusion and Air Pollution: Adv. Geophys.* **6**, 185–191.